Giant intrinsic magnetoresistance in spin-filtered tunnel junctions with ferrimagnetic electrode

Lalrinkima, S. M. Kastuar, L. Zadeng, R. Zosiamliana, B. Chettri, Y. T. Singh, L. Zuala, D. P. Rai, and C. E. Ekuma

Phys. Rev. B **107**, 155305 — Published 17 April 2023

DOI: 10.1103/PhysRevB.107.155305

Giant Intrinsic Magnetoresistance in Spin-Filtered Tunnel Junctions with Ferrimagnetic Electrode

Lalrinkima,[1,2] S. M. Kastuar,[3] L. Zadeng,[1] R. Zosiamliana,[4] B. Chettri,[4] Y. T. Singh,[4] L. Zuala,[4] D. P. Rai,[4,*] and C. E. Ekuma[3,5,†]

[1] *Department of Physics, Mizoram University, Aizawl-796009, India*
[2] *Pachhunga University College, Mizoram University, Aizawl-796001, India*
[3] *Department of Physics, Lehigh University, Bethlehem, PA 18015, USA*
[4] *Department of Physics, Pachhunga University College, Mizoram University, Aizawl-796001, India*
[5] *Institute for Functional Materials & Devices, Lehigh University, Bethlehem, PA 18015, USA*

(Dated: April 6, 2023)

In recent years, magnetic tunnel junctions (MTJs) have attracted strong research interest due to their potential use in nonvolatile memory technologies, such as magnetoresistive random access memory, and magnetic logic applications. Half-metallic materials have been proposed as ideal electrode materials for MTJs to achieve large tunnel magnetoresistance (TMR) effects. Here, we design and investigate a spin-filter MTJ (sf-MTJ) consisting of a ferrimagnetic inverse Heusler alloy, Mn_2CoSi as the electrode and CaS as the insulating tunnel barrier using *ab initio* quantum transport calculations. Our results demonstrate a high zero-bias voltage TMR ratio that initially oscillated before decreasing as the bias voltage increased. Despite the oscillatory TMR under bias voltage, the spin injection remains high and stable, highlighting the potential of sf-MTJs formed by Mn_2CoSi electrodes for practical applications.

I. INTRODUCTION

Magnetic tunnel junctions (MTJs) have garnered significant research attention in recent years due to their crucial role in the development of spintronics as they have a wide range of potential applications, including read-head sensors, nonvolatile memory devices such as STT MRAM and SOT MRAM, and nonvolatile logic and logic-in-memory computing.[1,2] However, designing magnetic materials that meet the requirements for high-performance spintronic devices, such as high spin polarization, high Curie temperature, low magnetic moment, and high tunneling magnetoresistance (TMR) ratio, is challenging due to the inefficiency of spin injection[3–6]. In the past two decades, significant advancements have been made in identifying material properties that optimize the design of spintronic devices beyond conventional magnetic tunnel diodes and transistors[7–14]. For example, spin-gapless semiconductors and half-metallic magnets have been incorporated into magnetic tunnel diode and transistor concepts, resulting in a substantial improvement in TMR ratio[10,15]. The use of ferromagnetic electrodes, such as Fe and Co, has enabled symmetric filtering, leading to improved TMR ratio.[9] However, compensated antiferromagnetic materials are currently preferred over ferromagnetic electrodes due to their faster information processing, robustness against perturbing magnetic fields, and spin-momentum coupling.[11–14]

Heusler alloys[16–20] have emerged as promising materials for designing high-performance MTJs due to their novel properties such as high Curie temperature.[21–28] Recent studies of MTJs based on Heusler compounds with MgO spaces have reported a high TMR ratio.[8,29] A fully epitaxial $Co_2Cr_{0.6}Fe_{0.4}Al/MgO/Co_{50}Fe_{50}$ MTJ exhibited a TMR ratio of 90 and 240% at room temperature and 4.2 K, respectively. By doping $Co_2MnSi/MgO/Co_2MnSi$ MTJs with Fe, Liu *et al.* reported an enhanced TMR ratio of ∼429% at 290 K[30]. Though some Heusler-based materials have shown high TMR ratios, their fabrication process cannot be improved further due to their high resistance area.[31] The main cause of this problem is the lattice mismatch at the contact with MgO that destroys the half-metallicity. To maintain a high TMR ratio while reducing the electrical resistance at the barrier interface, alternative tunneling materials need to be explored.

In this paper, we investigate the spin-dependent transport properties of magnetic tunnel junction consisting of the [001] CaS barriers sandwiched between two ferrimagnetic inverse Heusler alloy (IHA), Mn_2CoSi electrodes using first-principles quantum transport calculations. Mn-based inverse Heusler (Hg_2CuZ-type, with $Z = Al$, Ga, In, Si, Ge, Sn, Sb) alloy is promising for integration into MTJ devices due to their low saturation magnetization and half-metallic properties. Their electronic properties have been extensively studied.[32–38]. In particular, ferrimagnetic IHA Mn_2CoSi exhibits a robust half-metallicity over a wide range of structural tunability, within the lattice constant of the CaS barrier layer.[39] Ferrimagnetic half-metallic magnets electrodes in magnetic tunnel junctions offer unique advantages over conventional magnetic tunnel diodes and transistors, such as reconfigurability, while addressing limitations such as less asymmetric current-voltage characteristics in diodes, and base-collector leakage currents in transistors; these limitations often lead to high power dissipation. Despite their potential advantages, to the best of our knowledge, there have been no computational studies on the heterostructure configuration of Mn_2CoSi surfaces and interfaces and their incorporation as an electrode in MTJs. Further research utilizing first-principles calculations to

analyze the surface states and interfacial electronic properties is necessary for successful experimental synthesis and future studies. Our quantum transport calculations reveal a high zero-bias TMR ratio of ∼15000%, an oscillatory TMR ratio due to bias voltage, but stable spin injection efficiency.

II. COMPUTATIONAL METHOD

The face center cubic inverse Heusler Mn_2CoSi alloy crystallizes in the XA-structure (Hg_2CuTi-type) and belongs to space group $F\bar{4}3m$. The atomic position is described by the Wyckoff position: 4a (0, 0, 0), 4b (1/2, 1/2, 1/2), 4c (1/4, 1/4, 1/4), and 4d (3/4, 3/4, 3/4), where Mn atoms are located at 4b and 4d, Co and Si atoms occupy the 4a and 4c sites, respectively. Our *ab initio* calculations of Mn_2CoSi/CaS/Mn_2CoSi magnetic tunnel junction are based on spin-polarized density functional theory (DFT)[40] using the QuantumATK electronic structure code (version 2019.12SP1).[41] We employed linear combinations of atomic orbitals as the basis set together with the norm conversing pseudopotentials with the Perdew-Burke-Ernzerhof (PBE) parametrization of the exchange-correlation functional. To accurately account for the strong electron interactions in our system, we used an onsite effective Hubbard interaction (Ueff) within the DFT+U approximation, with a fully screened Coulomb and exchange interaction parameters (J) as follows: U_{Co} = 1.83 eV, J_{Co} = 0.53 eV, U_{Mn} = 1.71 eV, and J_{Mn} = 0.46 eV.[42]. The ground state properties are determined using a $12\times12\times12$ ($12\times12\times1$) Monkhorst-Pack k-point grid for the bulk ([001] surface) and a density mesh cutoff of 95 Hartree. The structural optimization is performed using the conjugate gradient algorithm by minimizing the energy and atomic forces until all the forces converge to at least 0.01 eV/Å and self-consistency is achieved when the energies between the two steps of the self-consistency field cycle differ by less than 10^{-6} eV. Two terminated MnSi and MnCo relaxed thin films of Mn2CoSi [001] with 13 diatomic layers were designed to determine the most stable configuration and termination. A 6 diatomic layer of CaS [001] and 11 layers of Mn_2CoSi [001] with Ca-Mn on top and Ca-Si on top configurations were designed for the interfacial heterostructures with CaS [001]. Because of the higher relaxation energy, we ignored the Ca-Si configuration. The quantum transport calculations are performed using the nonequilibrium Green's function (NEGF) approach[43,44] using a $10\times10\times200$ k-point mesh with a smearing of 26 meV and cutoff energy of 120 Hartree. To obtain the $I-V$ characteristics, QuantumATK employs the Landauer-Büttiker method,[45] $I(V) = (e/h)\sum_\sigma \int T^\sigma(E,V)[f_L(E,V) - f_R(E,V)]\,dE$, where $f_L(E,V)$ ($f_R(E,V)$) is the Fermi-Dirac distribution of the left (right) electrode, $T^\sigma(E,V)$ is the transmission coefficient, which depends on the spin σ of the electrons, an applied bias voltage V and energy E. For the calculation of the $T^\sigma(E,V)$, we choose a dense 200×200 k-point mesh to integrate the 2D Brillouin zone along the transverse Bloch wave vectors $\mathbf{K}_\parallel(k_A,k_B)$.

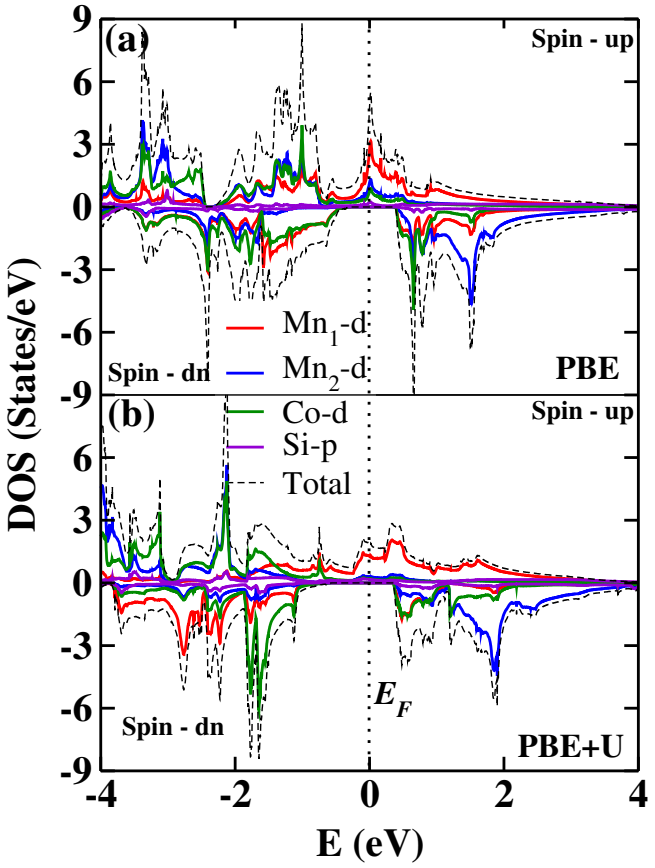

FIG. 1. Calculated spin polarized density of states and orbital projected density of states of bulk Mn_2CoSi obtained with (a) PBE and (b) PBE+U functional. The vertical dashed line is the Fermi energy.

III. RESULTS AND DISCUSSION

A. Bulk electronic and magnetic properties

To ensure the structural integrity of the electrode channel, we determine the lattice constants, magnetic moments of the bulk inverse Heusler alloy Mn_2CoSi using PBE functional. We obtained a lattice constant a of 5.62±0.10 Å and total magnetic moment of ∼ 3.0 μ_B. The calculated values are within the previous reported values of 5.4 - 5.9 Å[32,33,46] and 3.00 μ_B.[33] Detailed result of the lattice parameter calculations are in the Figure S1 and Table S1 in the Supplemental Material (SM).[47] We also verified the dynamical stability of the bulk structure by calculating the phonon dispersion and vibrational properties using density functional perturbation theory.[48] The absence of imaginary frequency confirms the dynamical stability of the structure (Figure S4[47]). We present in Figure 1 the calculated spin polarized elec-

tronic structure using PBE and PBE+U. We note that the magnetic moment of the two inequivalent Mn atoms (Mn_1 and Mn_2) is anti-parallel to each other with values of -0.75 (-1.99 μ_B) and 3.00 (3.88 μ_B) for Mn_1 (Mn_2) as obtained within our PBE and PBE+U calculations. The antiferromagnetic coupling between two Mn sub lattices with net nonzero total magnetic moment revealed the ferrimagnetic ground state of Mn_2CoSi; this is consistent with previous studies.[33,39,46] The spin-majority channel is characterized by a metallic solution, while the spin-minority channel has an energy bandgap of 0.83 and 0.89 eV within our PBE and PBE+U calculations. Our analysis shows that the minority spin gap originated from the strong hybridization between $Mn_2 - d$ states and its neighboring $Mn_1 - d$ and Co-d states. The wider bandgap of Mn_2 atom to Mn_1 and Co atoms supports larger exchange splitting induced by large localized spin moment on the Mn_2 site.[22] The strong hybridization between $Mn_2 - d$ and Co-d states led to the occupation of the bonding majority spin (↑) states, whereas the bonding minority spin (↓) states are mainly contributed by the $Mn_1 - d$ and Co-d states hybridizing with the t_{1u} states. An overlapping doubly degenerated e_u states of $Mn_1 - d$ and Co-d atoms occupied at the edges of the minority conduction bands in the minority spin channel. This suggests reasonably strong $d - d$ hybridization occurs only between Mn_1 and Co atoms. Thus, the half-metallicity is determined by a narrower $d - d$ bandgap of Mn_1 and Co atom over a wider covalent-like $Mn_2 - d$ bandgap. Interestingly, instead of the usual e_g-t_{2g} splitting of $d - d$ bandgap observed in full Heusler alloys, Mn_2CoSi bandgap is due to the energy splitting of the e_u-t_{1u} from the $d-d$ hybridization of Mn_1 and Co atoms. To determine the spin polarization at the Fermi level E_F, we use $P_s = [N_\uparrow(E_F) - N_\downarrow(E_F)]/[N_\uparrow(E_F) + N_\downarrow(E_F)]$, where $N_\uparrow(E_F)$ and $N_\downarrow(E_F)$ are the density of states at E_F. X_2YZ type Heusler alloys follow the Slater-Pauling rule: $\mu_t = Z_t - 24$, where μ_t is the total magnetic moment and Z_t is the total number of valence electrons.[22,49] The total magnetic moment for 27 total valence electron system of Mn_2CoSi is expected to be $\sim 3\,\mu_B$ in basic agreement with our computed value.

B. Surface structure and electronic properties

To understand the interfacial properties of ferrimagnetic IHA Mn_2CoSi/semiconductor heterostructure, we construct free-standing surface slabs of Mn_2CoSi [001]. To achieve this, we exfoliated two terminations: MnSi and MnCo from the optimized bulk structure using (1×1) supercell method. We modeled the slabs with 13 diatomic layers with a vacuum of 15 Å along the z-direction to prevent slab interactions. The generated in-plane lattice of the slabs is estimated with $a\sqrt{2}/2$, where a is the equilibrium lattice constant. In all the structural relaxation the top five layers are relaxed while the three core layers are fixed. The optimized structural and energetic properties of the two energetically favorable terminations are presented in Table I

TABLE I. The calculated optimized atomic displacement of the surface, subsurface, and third layer in the percentage of the equilibrium bulk lattice constant, surface energy γ (eV), the relaxation energy E_{rel} (eV), and the pressure P (GPa) exerted during the structural relaxation. See further details in Tables S2 & S3.[47]

Termination	Layer	d_{i-f}(%)	γ (eV)	E_{rel} (eV)	P(GPa)
MnSi	Mn_1/Si	3.35/-1.24	-2.40	-0.27	-1.17
	Mn_1/Co	-0.16/0.02			
	Mn_2/Si	0.26/0.50			
MnCo	Mn_1/Co	-1.13/-1.96	-2.31	-0.34	-1.10
	Mn_1/Si	1.54/1.02			
	Mn_2/Co	-0.03/-0.19			

In the MnSi termination, a minimal inward relaxation for the surface Si and an outward relaxation for the Mn_1 atoms led to a surface buckling of ∼0.26 Å. We attribute this to the surface and near-surface layer rearrangement of the valence displaced electrons,[50] which drove the ionic force towards the vacuum resulting in outward relaxation of the surface Mn atoms .[23,51] For MnCo terminated surface, both the surface Mn and Co atoms relax inward during the structural optimization. The negative values of pressure exerted by the systems during the relaxation indicated structural compression in both surface terminations. Based on the energetics characterized by the surface energy $\gamma = (E_{slab} - NE_{bulk})/2A$[52,53] and the relaxation energy E_{relax}, the MnSi termination is slightly more stable and preserves the half-metallicity predicted in the bulk.

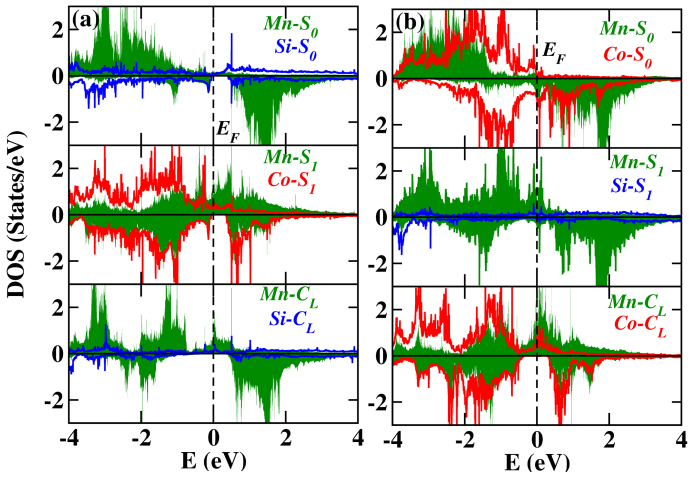

FIG. 2. Calculated spin polarized density of states of Mn_2CoSi [001] surface for the (a)MnSi and (b)MnCo terminations showing the atomic projected density of states of the dominant atoms in the surface layer S_0, subsurface layer S_1, and the central layer C_L.

We investigate the surface structure by analyzing the spin-polarized electronic structure characterized by the

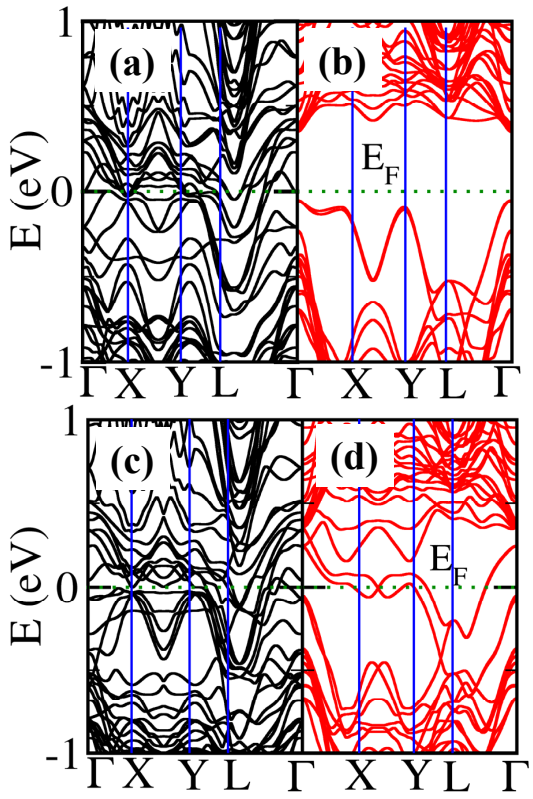

FIG. 3. Calculated spin polarized electronic band structure of Mn_2CoSi [001] surface for MnSi termination: (a) spin majority channel and (b) spin minority channel, and MnCo termination: (c) spin majority channel and (d) spin minority channel. The Fermi energy is represented by the horizontal dashed line.

density of states (Figure 2 and the dispersion spectra (Figure 3). The surface states in both terminations behaved differently. In the MnSi terminated surface, the half-metallicity is preserved with a minority spin (↓) direct energy bandgap around E_F and an adjacent metallic solution in the majority spin (↑) channel (Figures 2(a)& 3(a)). On the contrary, the MnCo terminated surface exhibited a gapless solution in both spin channels. Half-metallicity is lost at the surface due to the delocalization of Mn and Co d-states. However, the central region of the system maintains half-metallicity in both MnSi and MnCo terminations (see Figure 2), indicating that the slab thickness is sufficient to preserve strong magnetic and electronic properties in the bulk. Table S2 in the Supplemental Material[47] presents the calculated atomic-resolved magnetic moments for the surface and subsurface atoms. We see an increase in spin magnetic moments ($> 3.0\,\mu_B$) of surface Mn atoms in MnSi-terminated surfaces. The broken translational symmetry at the surface causes a rearrangement of valence electrons, leading to stronger intra-atomic exchange interactions and larger localized spin magnetic moments for surface Mn atoms as compared to the bulk. The anti-parallel spin moment of surface Si atoms slightly increases, likely due to direct exchange between the P-orbital of surface Si atoms and the d-orbital of subsurface Mn atoms. Subsurface Co atoms are less affected by the surface, showing a negligible change in the magnetic moment from the bulk value. In the MnCo-terminated surface, the Mn atoms in the third layer are terminated and we observe a parallel spin between the surface and subsurface Mn states, which is unexpected. We suspect that the antiparallel moment found in the subsurface Si atoms is caused mainly by the second subsurface Mn atoms. The intricate nature of the surface and subsurface magnetic states may be the result of a competition between direct exchange and antiferromagnetic superexchange interactions.

C. MTJ Device structure and Central region optimization

In this section, we examine the quantum spin transport properties of Mn_2CoSi/CaS/Mn_2CoSi magnetic tunnel junction device designed with Mn_2CoSi [001] electrodes and a semiconducting CaS [001] barrier layer. We selected CaS as the barrier layer because it not only shares the same crystal symmetry with Mn_2CoSi, but also maintains stable structural integrity over a wide range of lattice tunability (from ∼5.40 to 5.72 Å,[54–58]) which encompasses our calculated Mn_2CoSi lattice constant of ∼5.62 Å. This will significantly reduce interfacial resistance and increase the active area of the device. The interface is modeled by matching the two in-plane lattices using the coincidence site lattice method with an $nV_1 + mV_2$ grid size search, where V_1 and V_2 are the basis of the first lattice, and $-(n,m)^{max} \leq (m,n) \leq (n,m)^{max}$ are integers. We used a symmetric atomic termination with length 11.22 Å for both the left and right principal layer electrodes, and a length of 47.54 Å for the central region, maintaining an in-plane lattice constant of 3.97 Å throughout the device. Thus, the MTJ device can be said to be periodic in the $x-y$ plane and the z direction is the transport direction. The atomic positions of the central region are fully relaxed with an optimized Mn-Ca bond length of ∼ 2.52 Å. The schematic of the MTJ device is presented in Figure 4. The spin-dependent transport properties were then computed using NEGF for both unbiased voltage and the application of finite bias voltage.

The spin-dependent transport in magnetic tunnel junctions is driven by quantum mechanical tunneling. As a result, the characterization of the tunnel magnetoresistance ratio and the conductance (or the tunnel current) are crucial for device applications. In general, the resistance of these devices varies in two configurations: when the magnetization of the left and right electrodes is oriented parallel (P) and when it's switched to antiparallel (AP), resulting in the TMR effect. To explore these and gain further insight into the quantum spin transport of the designed MTJ, we compute the

TABLE II. The calculated spin-polarized quantum conductance (in Siemens) for parallel magnetization ($G^{\uparrow\uparrow}$, $G^{\downarrow\downarrow}$) and anti-parallel magnetization ($G^{\uparrow\downarrow}$, $G^{\downarrow\uparrow}$) configurations and total spin polarised current I_P^{Total}, I_{AP}^{Total} (in nA) for P and AP configurations.

Bias voltage (V)	$G^{\uparrow\uparrow}$	$G^{\downarrow\downarrow}$	$G^{\uparrow\downarrow}$	$G^{\downarrow\uparrow}$	I_P^{Total}	I_{AP}^{Total}	TMR ratio (%)
0.0	1.54×10^{-7}	1.17×10^{-10}	4.53×10^{-10}	4.51×10^{-10}	-	-	1.5×10^{4}
0.2	1.43×10^{-7}	1.05×10^{-10}	3.14×10^{-10}	3.35×10^{-8}	22.84	3.14	628
0.4	8.64×10^{-8}	2.61×10^{-10}	3.42×10^{-9}	1.75×10^{-7}	15.45	23.79	-35
0.6	1.26×10^{-7}	1.16×10^{-10}	3.75×10^{-10}	5.08×10^{-8}	79.08	12.56	529

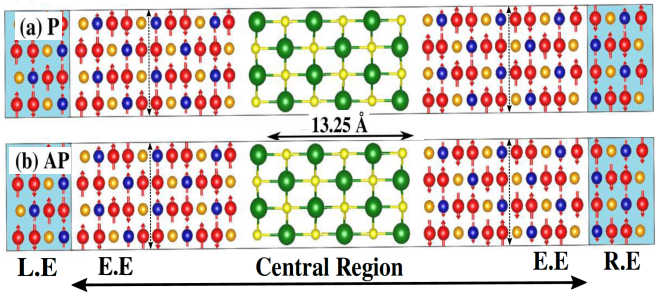

FIG. 4. Schematic representation of the magnetic tunnel junction device based on a ferrimagnetic inverse half-Heusler, half-metallic magnet and a semiconductor showing the initial spin degrees of freedom for (a) parallel configuration (P) and (b) antiparallel configuration (AP). $L.E(R.E)$ denotes the left(right) electrode and $E.E$ is electrode extension layer up to the dashed-$\updownarrow$for both the left and right electrodes.

transmission coefficient from the retarded Green's function as $T(E) = Tr\big[G(E)\Gamma^L(E)G^\dagger(E)\Gamma^R(E)\big]$,[59] where $G(E) = \big[(E+i\delta_+)S - H - \sum^L(E) - \sum^R(E)\big]^{-1}$ is the retarded Green's function matrix for the central region and $\Gamma^{L(R)} = (1/i)\big[\sum^{L(R)} - (\sum^{L(R)})^\dagger\big]$ is the broadening function of the electrodes. A ferrimagnetic MTJ device is more likely due to the ferrimagnetic ground state of the electrodes. As a result, the initial spin degrees of freedom are constrained to an antiferromagnetic configuration. The minority spin channel in the IHA ferrimagnetic Mn_2CoSi electrode has a gap near the Fermi energy, resulting in a zero transmission coefficient for minority spin electrons. As a result, the MTJ is in an "off" state, where no current flows through it when under forward bias. The transmission spectra (Figures 5) and consequently the $I-V$ curves (Figure 6) of the $Mn_2CoSi/CaS/Mn_2CoSi$ MTJ device can be explained based on the density of states (Figure 2). At zero temperature, when the magnetization directions of the electrodes are parallel, the majority spin electrons in the left IHA half-metallic electrode are blocked from tunneling through the insulating barrier layer into the right IHA half-metallic electrode due to the absence of states above the Fermi energy in the majority spin channel. The transport of minority spin electrons is also blocked as the electrode behaves like an insulator. A certain bias voltage is required for electron transport to occur. As a result, the tunneling current through the MTJ is fully (100%) spin-polarized. The same applies when the magnetization directions of the IHA half-metallic electrodes are oriented in an antiparallel manner. However, at finite temperatures, thermally activated electrons through processes such as non-spin flip stemming from e.g., spin-orbit coupling and electron-magnon interaction can be transmitted from one electrode to the other in the off states; this generally reduces the TMR ratios. We note that the non-spin-flip processes can be significantly reduced by increasing the bandgap of both the electrodes and the barrier. Our results indicate that, in the parallel configuration, the Fermi level has a small transmission coefficient with a spin-dependent transmission peak at ~1.8 eV above E_F for majority spin states. This originated from low-energy conduction states composed of Mn-d and Si-p states near the Γ point. However, the

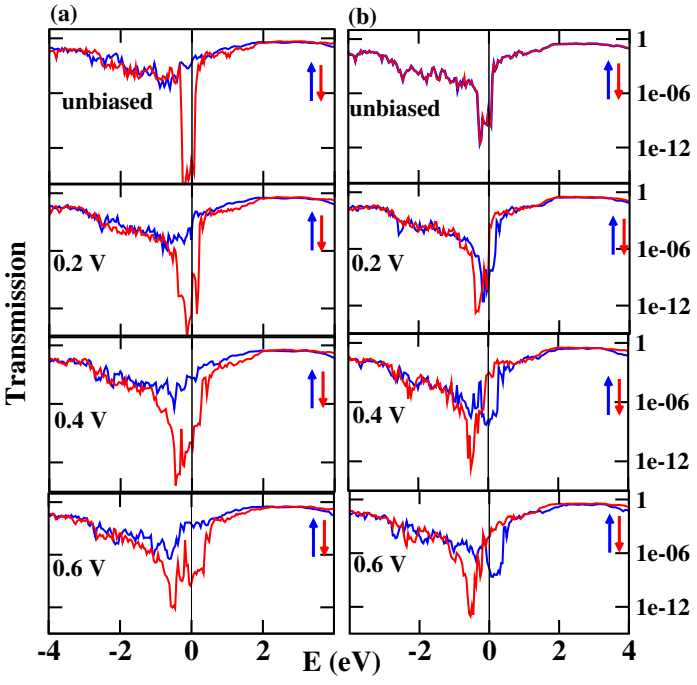

FIG. 5. Transmission coefficient (in log scale) as a function of bias voltage for parallel P (Left panel) and antiparallel AP (Right panel)-configuration within electron energy range -4 to 4 eV, direction of blue and red arrows indicate spin-up and spin-down states.

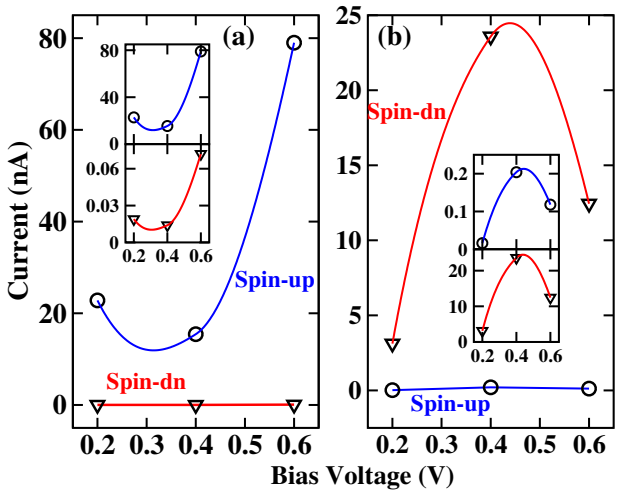

FIG. 6. The calculated I-V characteristic curve of the spin polarized current(nA) and bias voltage(V) for the (a) parallel and (b) antiparallel magnetic configurations. The insert is a zoomed view of the I-V curve.

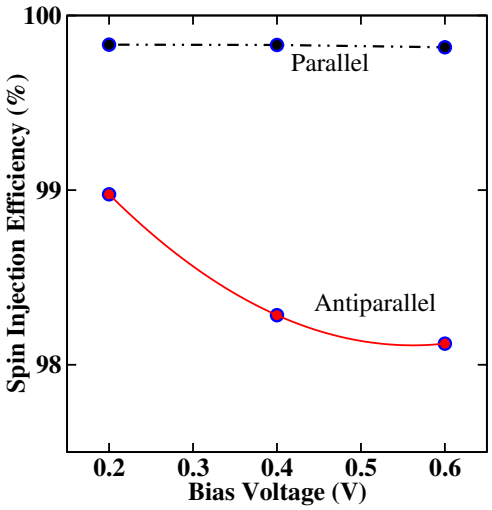

FIG. 7. The calculated spin injection efficiency (SIE) as a function of the bias voltage. The SIE remained high as the bias voltage was increased.

minority spin channel shows a sharp decrease in transmission probability near the Fermi level due to the half-metallic minority gap of the electrode, preventing any minority-spin Bloch states and resulting in coherent tunneling. However, in the antiparallel configuration, almost identical transmission curves (especially at zero bias voltage) are observed for both spin channels due to the mirror symmetry of the device. The symmetric nature is broken as the bias voltage is increased due to inelastic scattering emanating from the non-spin flip processes.[60] We can further quantify this by exploring the contour plots of the $K_{\|}(k_A,k_B)$ resolved transmission coefficient around Γ-point (Figures S6&S7[47]). A circularly polarized transmission is observed in both magnetic configurations and spin channels. However, as can be seen from the full 2D Brillouin zone, in the parallel configuration, in addition to the transmission around the zone center, there are other contributions from the special point in the vicinity of the 2D Brillouin zone edges (Figure S5). From our calculations, we can further infer that the current for both spin majority and minority channel in the parallel configuration initially decreased until 0.4 V before increasing with increasing bias voltage, but at different magnitudes (as seen in the inset of Figure 6(a)). The reverse in terms of trend is true in the antiparallel configuration where the current initially increased peaking at $\sim$ 0.4 V before decreasing monotonically with the bias voltage.

To determine the TMR, we first computed the spin-polarized quantum transport conductance $G^{\uparrow\uparrow}$ and $G^{\downarrow\uparrow}$ for both the parallel and antiparallel magnetic configurations (Table II). Using the conductance, we compute the TMR (within the optimistic approach) as TMR= $(G_p - G_{ap})/G_{ap}$, where G_p and G_{ap} are the conductance in parallel and antiparallel configurations, respectively (Table II). Note that for finite bias, the conductance is replaced with the equivalent tunneling current through the device.[61,62] Due to the large difference $\sim$ 3 orders of magnitude of the conductance between the parallel and antiparallel configurations, we obtain large tunneling magnetoresistance $\approx 1.5 \times 10^4$ % at zero-bias voltage. The conductance experiences a substantial reduction of up to 2 orders of magnitude at finite bias voltage. At a bias voltage of 0.4 V, the conductance of the spin majority states increases rapidly, resulting in an unusual oscillatory behavior that produces a negative TMR effect. Although such oscillatory TMR effects are typically observed in structurally asymmetric junctions independent of the bias voltage,[63] our design features symmetric electrodes, leading us to attribute the oscillating tunneling conductance under bias voltage to a nonmonotonic energy dependence of the transmission coefficients that splits the molecular field of the electrode.[64] This phenomenon occurs when the barrier at the insulator-electrode interface decreases at a certain bias voltage, causing partial over-barrier transfer and fluctuations in the transmission coefficient at energies below the barrier height. The barrier height and width, as well as the likelihood of over-barrier transmission, are influenced by the magnetization direction of the ferrimagnetic electrode and the relative orientation of the magnetic moments of the two electrodes. The magnitude of the TMR oscillation is approximately 10^3. Despite the oscillating behavior of the TMR ratio, it is noteworthy that the spin injection efficiency $S_e = |\frac{I^{\uparrow}-I^{\downarrow}}{I^{\uparrow}+I^{\downarrow}}| \times 100\%$ remained relatively high with increasing bias voltage. In the parallel configuration, the spin injection efficiency is constant with increasing bias voltage while in the antiparallel configuration, it is within 98 - 99% (Figure 7).

IV. CONCLUSION

In conclusion, our first-principle calculations of the ferrimagnetic inverse Heusler alloy, Mn_2CoSi, demonstrate its potential as a promising electrode in magnetic tunnel junction (MTJ) devices. Our calculations show that the half-metallic character of Mn_2CoSi is retained only along the [001] MnSi-terminated surface, making it a suitable candidate for spin injection. Our quantum spin transport calculations show that the designed MTJ device with $Mn_2CoSi/CaS/Mn_2CoSi$ exhibits a large tunnel magnetoresistance (TMR) at equilibrium and an oscillating TMR under a finite bias voltage. Despite this oscillation, our calculations reveal that the spin injection efficiency remains relatively constant in the parallel configuration and only changes by less than 1% (98.20 - 98.92%) in the antiparallel configuration. These results highlight the potential of half-metallic, ferrimagnetic inverse Heusler alloys as spin injectors for further exploration of tunneling anisotropic magnetoresistance, spin texture, and spin dynamics for potential spintronic applications. The half-metallic nature of Mn_2CoSi along with its large TMR value and constant spin injection efficiency make it a promising material for further investigation and characterization in experimental studies.

V. ACKNOWLEDGEMENTS

Lalrinkima acknowledges the Department of Science and Technology, New Delhi, India for INSPIRE Fellowship. CEE acknowledges the Lehigh University startup grant and NSF grant DMR-2202101. SMK acknowledges the Lee Graduate Fellowship from College of Arts and Sciences, Lehigh University. Supercomputer support is provided by the CCT@Lehigh.

* dibyaprakashrai@gmail.com
† che218@lehigh.edu

[1] S. K. Kingra, V. Parmar, C.-C. Chang, B. Hudec, T.-H. Hou, and M. Suri, Scientific Reports **10**, 2567 (2020).
[2] R. De Rose, T. Zanotti, F. M. Puglisi, F. Crupi, P. Pavan, and M. Lanuzza, Solid-State Electronics **184**, 108065 (2021).
[3] S. A. Wolf, D. D. Awschalom, R. A. Buhrman, J. M. Daughton, S. Von Molnár, M. L. Roukes, A. Y. Chtchelkanova, and D. M. Treger, Science (80-.). **294**, 1488 (2001).
[4] T. Dietl, H. Ohno, F. Matsukura, J. Cibert, and D. Ferrand, Science (80-.). **287**, 1019 (2000).
[5] I. Žutić, J. Fabian, and S. D. Sarma, Rev. Mod. Phys. **76**, 323 (2004), arXiv:0405528 [cond-mat].
[6] S. D. Bader and S. S. Parkin, Annu. Rev. Condens. Matter Phys. **1**, 71 (2010).
[7] T. Marukame, T. Ishikawa, K. I. Matsuda, T. Uemura, and M. Yamamoto, Appl. Phys. Lett. **88**, 262503 (2006).
[8] H. X. Liu, Y. Honda, T. Taira, K. I. Matsuda, M. Arita, T. Uemura, and M. Yamamoto, Appl. Phys. Lett. **101**, 132418 (2012).
[9] W. Butler, X.-G. Zhang, T. Schulthess, and J. MacLaren, Physical Review B **63**, 054416 (2001).
[10] E. Şaşıoğlu, S. Blügel, and I. Mertig, ACS Applied Electronic Materials **1**, 1552 (2019), https://doi.org/10.1021/acsaelm.9b00318.
[11] V. Baltz, A. Manchon, M. Tsoi, T. Moriyama, T. Ono, and Y. Tserkovnyak, Reviews of Modern Physics **90**, 015005 (2018).
[12] T. Jungwirth, X. Marti, P. Wadley, and J. Wunderlich, Nature nanotechnology **11**, 231 (2016).
[13] T. Jungwirth, J. Sinova, A. Manchon, X. Marti, J. Wunderlich, and C. Felser, Nature Physics **14**, 200 (2018).
[14] D.-F. Shao, S.-H. Zhang, M. Li, C.-B. Eom, and E. Y. Tsymbal, Nature Communications **12**, 7061 (2021).
[15] N. Maji and T. K. Nath, Applied Physics Letters **120**, 072401 (2022), https://doi.org/10.1063/5.0077607.
[16] F. Heusler, "Verhandl. Deut. Physik. Ges. 5, 219 (1903). - Google Scholar," (1903).
[17] A. A. Knowlton and O. C. Clifford, Trans. Faraday Soc. **8**, 195 (1912).
[18] D. P. Oxley, R. S. Tebble, and K. C. Williams, J. Appl. Phys. **34**, 1362 (1963).
[19] P. J. Webster, Contemp. Phys. **10**, 559 (2006).
[20] T. Graf, C. Felser, and S. S. Parkin, Prog. Solid State Chem. **39**, 1 (2011).
[21] S. Wurmehl, G. H. Fecher, H. C. Kandpal, V. Ksenofontov, C. Felser, and H. J. Lin, Appl. Phys. Lett. **88**, 032503 (2006), arXiv:0511462 [cond-mat].
[22] I. Galanakis, J. Phys. Condens. Matter **14**, 6329 (2002).
[23] S. J. Hashemifar, P. Kratzer, and M. Scheffler, Phys. Rev. Lett. **94** (2005), 10.1103/PHYSREVLETT.94.096402/FIGURES/1/THUMBNAIL.
[24] H. C. Kandpal, G. H. Fecher, C. Felser, and G. Schönhense, Phys. Rev. B **73**, 094422 (2006).
[25] K. Inomata, N. Ikeda, N. Tezuka, R. Goto, S. Sugimoto, M. Wojcik, and E. Jedryka, Sci. Technol. Adv. Mater. **9**, 14101 (2008).
[26] L. Siakeng, G. M. Mikhailov, and D. P. Rai, J. Mater. Chem. C **6**, 10341 (2018).
[27] S. K. Bose, J. Kudrnovský, V. Drchal, and I. Turek, Phys. Rev. B - Condens. Matter Mater. Phys. **84**, 174422 (2011).
[28] D. P. Rai, Lalrinkima, Lalhriatzuala, L. A. Fomin, I. V. Malikov, A. Sayede, M. P. Ghimire, R. K. Thapa, and L. Zadeng, RSC Adv. **10**, 44633 (2020).
[29] T. Ishikawa, H. X. Liu, T. Taira, K. I. Matsuda, T. Uemura, and M. Yamamoto, Appl. Phys. Lett. **95**, 232512 (2009).
[30] H. X. Liu, T. Kawami, K. Moges, T. Uemura, M. Yamamoto, F. Shi, and P. M. Voyles, J. Phys. D. Appl. Phys. **48**, 164001 (2015).
[31] K. Elphick, W. Frost, M. Samiepour, T. Kubota, K. Takanashi, H. Sukegawa, S. Mitani, and A. Hirohata, Sci. Technol. Adv. Mater. **22**, 235 (2021).
[32] N. Maji and T. K. Nath, J. Appl. Phys. **125**, 173903 (2019).
[33] V. V. On, D. K. Nguyen, D. M. Hoat, R. Ponce-Pérez, J. F. Rivas-Silva, and G. H. Cocoletzi, Int. J. Quantum

Chem. **121**, e26445 (2021).
[34] I. Galanakis, K. Özdoğan, E. Şaşioğlu, and B. Aktaş, Phys. Rev. B - Condens. Matter Mater. Phys. **75**, 092407 (2007).
[35] G. D. Liu, X. F. Dai, H. Y. Liu, J. L. Chen, Y. X. Li, G. Xiao, and G. H. Wu, Phys. Rev. B - Condens. Matter Mater. Phys. **77**, 014424 (2008).
[36] C. Jiang, M. Venkatesan, and J. M. Coey, Solid State Commun. **118**, 513 (2001).
[37] K. Ramesh Kumar, N. Harish Kumar, G. Markandeyulu, J. A. Chelvane, V. Neu, and P. D. Babu, J. Magn. Magn. Mater. **320**, 2737 (2008).
[38] H. Wu, G. Vallejo-Fernandez, and A. Hirohata, J. Phys. D. Appl. Phys. **50**, 375001 (2017).
[39] N. Xing, H. Li, J. Dong, R. Long, and C. Zhang, Comput. Mater. Sci. **42**, 600 (2008).
[40] W. Kohn and L. J. Sham, Phys. Rev. **140**, A1133 (1965).
[41] S. Smidstrup, T. Markussen, P. Vancraeyveld, J. Wellendorff, J. Schneider, T. Gunst, B. Verstichel, D. Stradi, P. A. Khomyakov, U. G. Vej-Hansen, M. E. Lee, S. T. Chill, F. Rasmussen, G. Penazzi, F. Corsetti, A. Ojanperä, K. Jensen, M. L. Palsgaard, U. Martinez, A. Blom, M. Brandbyge, and K. Stokbro, J. Phys. Condens. Matter **32**, 015901 (2019), arXiv:1905.02794.
[42] E. Şaşioğlu, I. Galanakis, C. Friedrich, and S. Blügel, Phys. Rev. B - Condens. Matter Mater. Phys. **88**, 134402 (2013).
[43] D. Stradi, U. Martinez, A. Blom, M. Brandbyge, and K. Stokbro, Phys. Rev. B **93**, 155302 (2016), arXiv:1601.04651.
[44] J. M. Marmolejo-Tejada, K. Dolui, P. Lazić, P. H. Chang, S. Smidstrup, D. Stradi, K. Stokbro, and B. K. Nikolić, Nano Lett. **17**, 5626 (2017), arXiv:1701.00462.
[45] M. Büttiker, Y. Imry, R. Landauer, and S. Pinhas, Phys. Rev. B **31**, 6207 (1985).
[46] M. Singh, H. S. Saini, J. Thakur, A. H. Reshak, and M. K. Kashyap, J. Solid State Chem. **208**, 71 (2013).
[47] See Supplemental Material at [URL will be inserted by publisher]. The structural, elastic constants, and quantum transport properties of bulk, surface [001], and $Mn_2CoSi/CaS/Mn_2CoSi$ magnetoresistance tunneling junction.
[48] M. Gajdoš, K. Hummer, G. Kresse, J. Furthmüller, and F. Bechstedt, Phys. Rev. B **73**, 045112 (2006).
[49] S. Skaftouros, K. Özdoğan, E. Şaşıoğlu, and I. Galanakis, Phys. Rev. B **87**, 024420 (2013).
[50] V. Chis and B. Hellsing, Phys. Rev. Lett. **93**, 226103 (2004).
[51] Lalrinkima, C. E. Ekuma, T. C. Chibueze, L. A. Fomin, I. V. Malikov, L. Zadeng, and D. P. Rai, Phys. Chem. Chem. Phys. **23**, 11876 (2021).
[52] I. Galanakis, N. Papanikolaou, and P. H. Dederichs, Surf. Sci. **511**, 1 (2002), arXiv:0110236 [cond-mat].
[53] I. Galanakis, G. Bihlmayer, V. Bellini, N. Papanikolaou, R. Zeller, S. Blügel, and P. H. Dederichs, Europhys. Lett. **58**, 751 (2002), arXiv:0105207 [cond-mat].
[54] M. M. Abdus Salam, Results Phys. **10**, 934 (2018).
[55] Z. Charifi, H. Baaziz, F. El Haj Hassan, and N. Bouarissa, J. Phys. Condens. Matter **17**, 4083 (2005).
[56] H. Luo, R. G. Greene, K. Ghandehari, T. Li, and A. L. Ruoff, Phys. Rev. B **50**, 16232 (1994).
[57] M. Bayrakci, K. Colakoglu, E. Deligoz, and Y. O. Ciftci, High Press. Res. **29**, 187 (2009).
[58] G. K. Straub and W. A. Harrison, Phys. Rev. B **39**, 10325 (1989).
[59] D. E. Petersen, H. H. B. Sørensen, P. C. Hansen, S. Skelboe, and K. Stokbro, J. Comput. Phys. **227**, 3174 (2008).
[60] S. Zhang, P. M. Levy, A. C. Marley, and S. S. Parkin, Phys. Rev. Lett. **79**, 3744 (1997).
[61] Y. Feng, Z. Cui, M. sheng Wei, and B. Wu, Appl. Surf. Sci. **466**, 78 (2019).
[62] E. Montes, I. Rungger, S. Sanvito, and U. Schwingenschlögl, New J. Phys. **18**, 113024 (2016).
[63] C. Heiliger, P. Zahn, B. Y. Yavorsky, and I. Mertig, Phys. Rev. B **73**, 214441 (2006).
[64] A. S. Panfilenok, A. L. Danilyuk, and V. E. Borisenko, Tech. Phys. 2008 **53**, 479 (2008).